ACADEMIC
PRESS

Available online at www.sciencedirect.com

SCIENCE DIRECT®

Journal of Sound and Vibration 266 (2003) 407–441

JOURNAL OF
SOUND AND
VIBRATION

www.elsevier.com/locate/jsvi

Vibro-acoustic analysis procedures for the evaluation of the sound insulation characteristics of agricultural machinery cabins

W. Desmet*, B. Pluymers, P. Sas

Department of Mechanical Engineering, Division PMA, K.U. Leuven,
Celestijnenlaan 300B, B-3001 Leuven (Heverlee), Belgium

Received 13 January 2003

Abstract

Over the last few years, customer demands regarding acoustic performance, along with the tightening of legal regulations on noise emission levels and human exposure to noise, have made the noise and vibration properties into important design criteria for agricultural machinery cabins. In this framework, both experimental analysis procedures for prototype testing as well as reliable numerical prediction tools for early design assessment are compulsory for an efficient optimization of the cabin noise and vibration comfort.

This paper discusses several numerical approaches, which are based on the finite element and boundary element method, in terms of their practical use for airborne sound insulation predictions. To illustrate the efficiency and reliability of the various vibro-acoustic analysis procedures, the numerical procedures are applied for the case of a harvester driver's cabin and validated with experimental results.

1. Introduction

The high noise and vibration levels, to which drivers of agricultural machinery are often exposed for long periods of time, have a significant part in the driver's fatigue and may lead to substantial hearing impairment and health problems. For these reasons, the noise and vibration comfort has become an important criterion in the design of the driver's cabin and a determining factor in the acceptance and sales potential of agricultural machinery. Therefore, it is essential for an optimal cabin design to have time and cost effective analysis tools for the assessment of the

---

*Corresponding author. Tel.: +32-16-32-25-27; fax: +32-16-32-29-87.
E-mail address: wim.desmet@mech.kuleuven.ac.be (W. Desmet).

0022-460X/03/$ - see front matter © 2003 Elsevier Ltd. All rights reserved.
doi:10.1016/S0022-460X(03)00576-5

noise and vibration characteristics of various design alternatives at both the early design stages and the prototype-testing phase.

Two types of dynamic cabin excitations cause the interior noise in a driver's cabin. Airborne excitation consists of sound that impinges on the exterior of the cabin and introduces cabin vibrations, which transmit sound to the interior. Typical airborne noise sources in agricultural machinery such as harvesters are the engine, the feeder, the threshing unit and auxiliary equipment like pumps and compressors. Structure-borne excitation consists of dynamic forces, which are directly transmitted to the cabin through the cabin suspension. These transmitted forces introduce cabin vibrations, which in turn generate interior noise.

This paper outlines both an experimental analysis tool as well as some numerical modelling procedures, which can be used for the evaluation of the airborne sound insulation characteristics of a cabin. The tool for the measurement of the airborne sound insulation is based on sound pressure measurements and characterizes the sound insulation by the pressure insertion loss. In addition to the experimental tool for physical prototype testing, some numerical counterparts for virtual prototype testing are addressed. Various numerical modelling procedures, which are based on the finite element and boundary element method, are discussed and evaluated in terms of their accuracy and associated computational loads for calculating the airborne sound insulation properties of a cabin scale model. To illustrate the practical use of the described numerical methods in case of real-life structures, the most efficient method is also applied on a real harvester driver's cabin.

2. Harvester driver's cabin and scale model

The various sound insulation analysis tools, which are discussed throughout the paper, have been evaluated for a simplified scale model of an agricultural machinery driver's cabin. Compared to the real driver's cabin (see Fig. 1), the geometry of the scale model has been kept simple (see Fig. 2) in order to minimise the computational efforts, involved with the numerical analysis tools. The cabin scale model consists of five flat, trapezoidally shaped panels, glued together as shown in Fig. 2. All panels have different thicknesses and are made of different types of plexiglass material to simulate the distinct structural parts of a cabin (roof, floor, doors, windscreen, …), each having different dynamic characteristics. The thicknesses and the material properties are summarized in Table 1. The panel areas of the scale model are listed in Table 2, together with the corresponding cabin component areas. Because of the linear geometric scaling factor of ±2.5 to 1, the enclosed cabin volume of the scale model is reduced and the resonance frequencies of the scale model are shifted towards higher frequencies, when compared to the resonance frequencies of the real driver's cabin. Table 3 gives an overview of the first acoustic resonance frequencies, measured on the scale model cavity and the real cabin cavity. The scale model is placed in small grooves in a rubber mat, which is placed on the rigid floor of a semi-anechoic test room. The slits between the panels and the grooves are filled with silicone to acoustically seal the interior cavity.

The scale model panels have been designed such that, in a similar way as a real driver's cabin, they exhibit already a fairly high structural modal density (470 modes < 500 Hz) and structural damping (±3%) in the low-frequency audio range, as is shown in Table 4. Note that the high

Fig. 1. Harvester driver's cabin.

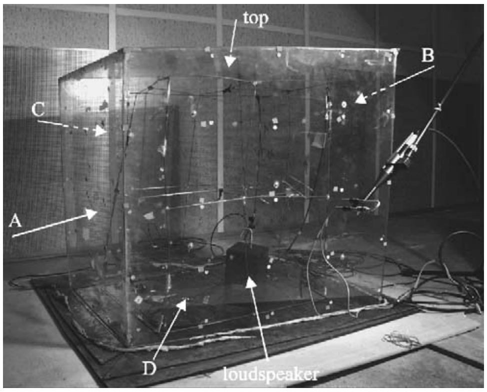

Fig. 2. Cabin scale model.

Table 1
Material properties of the scale model panels

Panel	E (N/m^2)	Density (kg/m^3)	Thickness (m)
A	2.3×10^9	1138	3.0×10^{-3}
B	4.6×10^9	1208	2.3×10^{-3}
C	1.8×10^9	1217	6.0×10^{-3}
D	1.8×10^9	1217	6.0×10^{-3}
Top	2.9×10^9	1309	2.3×10^{-3}

Table 2
Area of cabin components

Component of harvester	Area (m^2)	Panel of scale model	Area (m^2)	Linear scaling factor
Windscreen	3.8	A	0.48	2.8
Backside	3.8	B	0.68	2.4
Left/right side	3.2	C/D	0.62	2.3
Roof	3.0	Top	0.64	2.2

Table 3
Measured acoustic resonance frequencies (Hz)

Real cabin	Scale model
99.66	221.92
108.53	241.46
144.47	315.67
166.17	336.43

Table 4
Structural modes of cabin components

	Real cabin	Scale model
First structural mode	±10 Hz	±10 Hz
100th structural mode	78 Hz	135 Hz
Number of modes $<$ 250 Hz	900	215
Number of modes $<$ 500 Hz		470
Modal damping	±3%	±3%

number of structural modes of the real cabin (900 modes $<$ 250 Hz) is due to the high number of local modes of subcomponents of the cabin, like for instance the interior trim panels.

The frequency range of practical interest for studying the airborne sound insulation characteristics of the harvester driver's cabin is the 40–175 Hz frequency band, being the dominant band in the spectrum of the main airborne noise sources. Given the geometrical scaling factor, the frequency range of 40–350 Hz is considered for the cabin scale model analysis.

3. Insertion loss

A conventional way to experimentally identify the airborne sound insulation properties of a driver's cabin, is to disassemble the cabin and to measure the sound transmission loss of the various cabin components in a standard transmission suite test [1]. This paper describes, however, an alternative method to quantify the airborne sound insulation properties of a driver's cabin. The

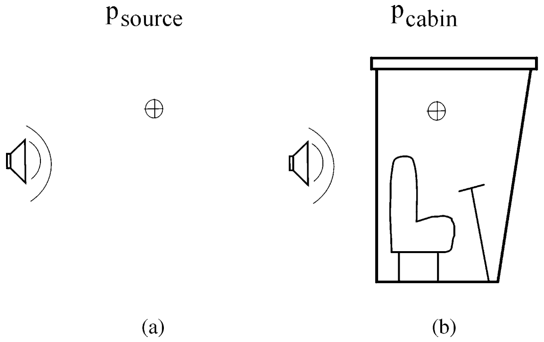

Fig. 3. Direct *IL* measurement layout.

method is based on the measurement of the cabin pressure insertion loss, which does not require the disassembly of the cabin.

The pressure insertion loss (*IL*) of a cabin is defined as the logarithmic ratio between the sound pressure p_{source} in a point at a certain distance from an acoustic source (see Fig. 3(a)), and the sound pressure p_{cabin} in that same point, when it is enclosed by the cabin, while the acoustic source remains at its same position outside the cabin (see Fig. 3(b)),

$$IL = 20 \log\left(\frac{p_{source}}{p_{cabin}}\right). \tag{1}$$

A positive *IL* indicates that the pressure level in the measurement point is reduced by the presence of the cabin, whereas a negative insertion loss indicates sound pressure amplification by the cabin.

The procedure for the insertion loss measurement, as outlined above, has been applied for the real harvester driver's cabin. The dynamic pressure responses in certain points inside the cabin, due to a broadband acoustic source excitation, located outside the cabin, are measured, as well as the pressure responses in the same measurement points, due to the same source excitation, but without the presence of the enclosing cabin structure. The measurements are performed on a driver's cabin which is dismounted from the harvester and fixed to a supporting frame structure, as shown in Fig. 1.

Fig. 4 shows the measured *IL* of the cabin, according to Eq. (1), for three points inside the cabin (one at the driver's left ear, one above the floor and one to the right of the driver, at arm's height), with an acoustic source located behind the cabin. At this position, the source represents the acoustic loading from the threshing unit, which, on a real harvester, is located behind the cabin. This figure shows that, for the lower frequencies (< 50 Hz), the *IL* is independent of the position of the measurement point inside the cabin while, at higher frequencies, the *IL* becomes dependent on the position of the measurement point. For confidentiality reasons, the ordinate legend has been omitted on all *IL* figures in this paper. All figures have, however, the same ordinate axis range, so that the different figures can be compared with each other.

Fig. 5 shows the measured *IL* for the same three points inside the cabin, but with an acoustic source in front of the cabin, representing the noise coming from the feeder installation. As in Fig. 4, the *IL* is independent of the position of the measurement point in the lower frequency range, while at higher frequencies, the *IL* again becomes position-dependent. Fig. 6 compares the

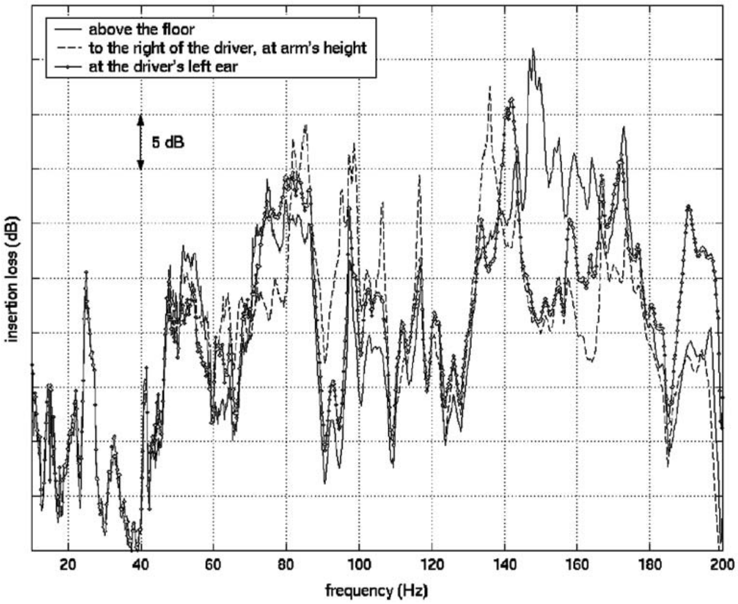

Fig. 4. *IL* measurements at different points in the cabin with a source behind the cabin.

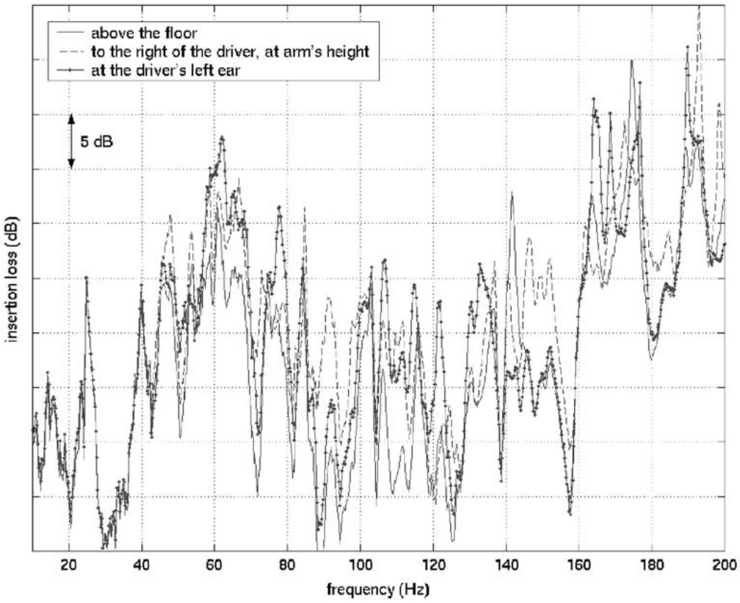

Fig. 5. *IL* measurements at different points in the cabin with a source in front of the cabin.

IL curves for the interior measurement point near the driver's left ear, for the source positions behind and in front of the cabin. These curves show that the *IL* also depends on the position of the acoustic source. Fig. 7 shows the difference between the two *IL* curves, i.e. the *IL* for the source

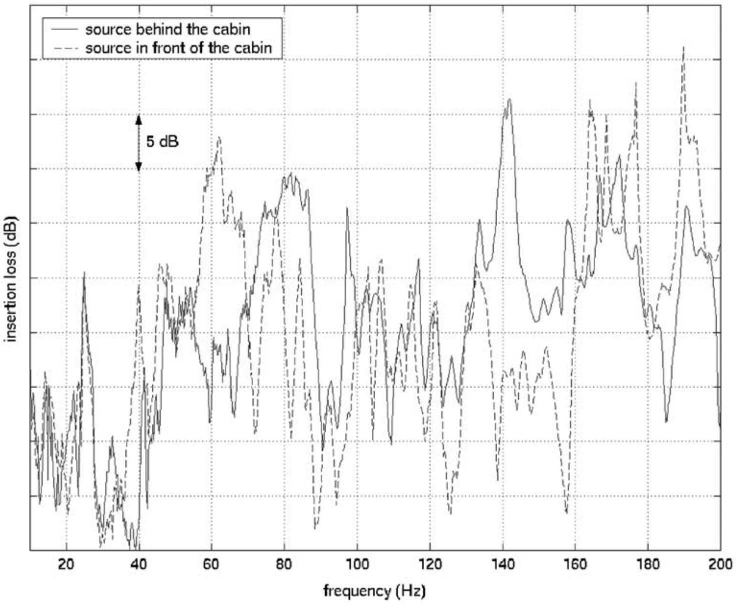

Fig. 6. *IL* measurements at the driver's left ear for different source positions.

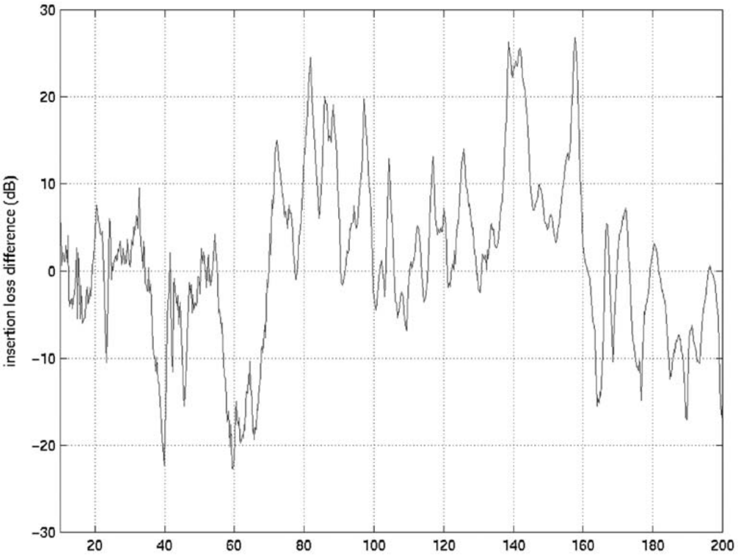

Fig. 7. *IL* measurements at the driver's left ear: difference between the *IL* for a source behind and in front of the cabin.

behind the cabin minus the *IL* for the source in front of the cabin. This figure indicates that in the low- (<75 Hz) and in the high-frequency range (>160 Hz) the cabin is a better isolator for noise sources in front of the cabin than for noise sources behind the cabin, while the opposite is true in the mid-frequency range (>75 Hz and <160 Hz).

To investigate the dependency of the *IL* (at the driver's ear) on the position of the acoustic source, several measurements have to be performed, each time changing the position of the outside source. Such a dependency-analysis is a useful, but time consuming tool to determine the *IL* for the acoustic loading from various regions on the harvester. By using a reciprocal measurement scheme, these different measurements can all be performed in one measurement run.

The following relationship expresses the vibro-acoustic reciprocity [2]:

$$\left.\frac{p_i}{\dot{q}_j}\right|_{\dot{q}_i=0} = \left.\frac{p_j}{\dot{q}_i}\right|_{\dot{q}_j=0}. \tag{2}$$

A possible interpretation of this reciprocity is that, when two cavities $C1$ and $C2$ are considered, which are separated from each other by means of a flexible structure, the ratio between the acoustic pressure response p_i at response location i in cavity $C1$ and the acoustic volume acceleration $\dot{q}_j$ at position j in cavity $C2$, without an acoustic volume acceleration excitation $\dot{q}_i$ in cavity $C1$, equals the ratio between the acoustic pressure response p_j at response location j in cavity $C2$ and the acoustic volume acceleration $\dot{q}_i$ at position i in cavity $C1$, without an acoustic volume acceleration excitation $\dot{q}_j$ in cavity $C2$.

Application of the reciprocity relation (2) to the *IL* definition, given in expression (1), yields a second, reciprocal definition for the *IL*. The pressure insertion loss of a cabin is then defined as the logarithmic ratio between the sound pressure p_{source} in a point at a certain distance of an acoustic source (see Fig. 8(a)), and the sound pressure p_{cabin} in that same point outside the cabin, while the acoustic source is enclosed by the cabin (see Fig. 8(b)). In the following discussions, the first definition (Fig. 3) will be denoted as the *direct IL* definition, while the second one (Fig. 8) will be denoted as the *reciprocal IL* definition.

It follows from Eq. (2) that the two definitions of the *IL* are only equivalent, provided that the volume acceleration of the sources in the two pressure measurement-setups (see Figs. 3 and 8), is exactly the same. In practice, however, the acoustic volume acceleration that results from driving a loudspeaker with a certain electrical signal is also dependent on the acoustic impedance of the environment in which the source is located. By moving the loudspeaker from an outdoor location (Fig. 3(b)) to an indoor location (Fig. 8(b)), the acoustic impedance, seen by the source, changes. Fig. 9 illustrates this effect. The full line represents the pressure measured at a point inside the cabin, due to an acoustic source excitation, which is located outside the cabin. The dashed

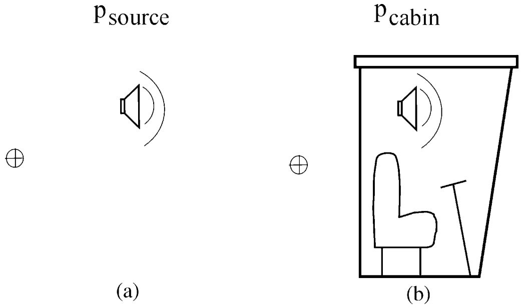

(a) (b)

Fig. 8. Reciprocal *IL* measurement layout.

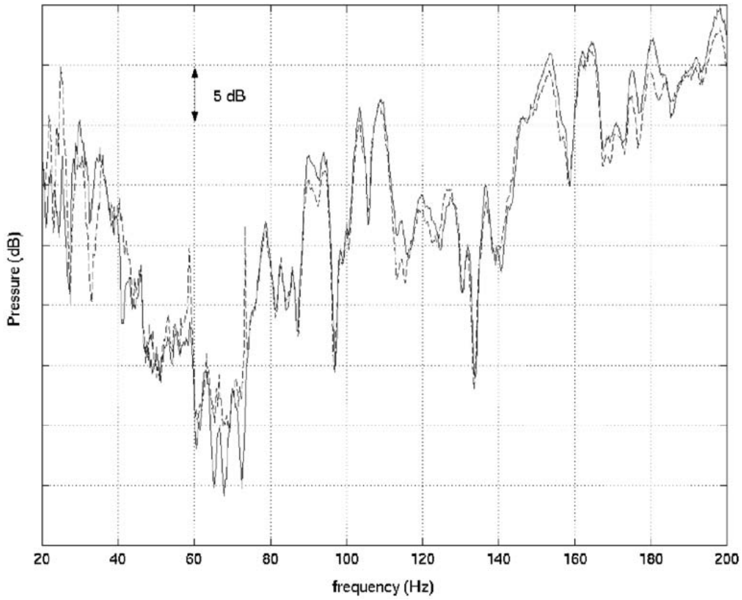

Fig. 9. Pressure responses (full line: measurement point inside the cabin and source outside; dashed line: measurement point outside the cabin and source inside).

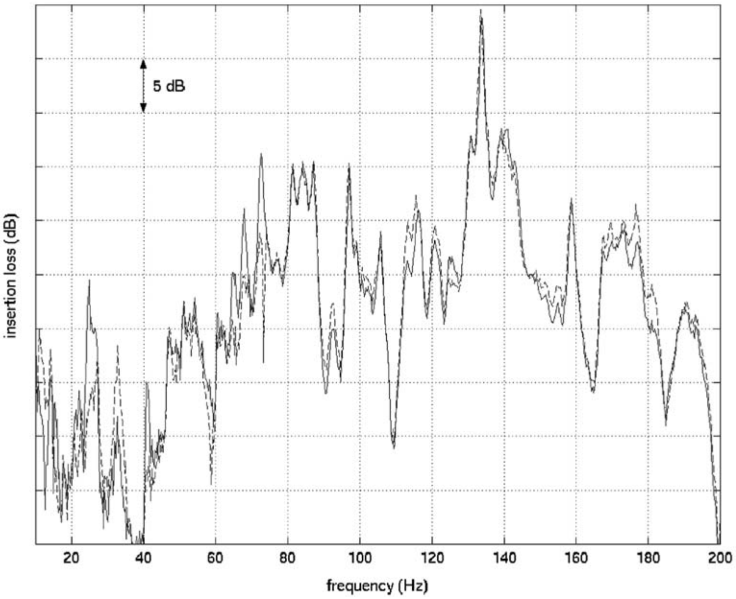

Fig. 10. Direct (solid line) and reciprocal *IL* (dashed line).

line represents the pressure response when the microphone position and the source position are interchanged. If there would be no impedance change, the two measurement curves should match perfectly according to Eq. (2). However, some differences can be noticed. Fig. 10 shows the corresponding *direct IL* (solid line) and the *reciprocal IL* (dashed line). The difference is acceptable for the considered measurements.

Applying the reciprocal measurement scheme, as shown in Fig. 8, facilitates the *IL* procedure in that for instance a sound source can be located at the driver's ear position, while the resulting pressures are (simultaneously) measured at various possible noise source locations around the harvester. This is more convenient than putting the sound source at various locations and measuring the resulting pressure at the driver's ear.

The reciprocal *IL* definition will also be validated in the numerical procedures. The method to model the acoustic source and the effect of the acoustic impedance of the environment will be discussed in more detail in Sections 4 and 5.

4. Numerical prediction tools

4.1. Introduction

A major imperative for reducing the design time and cost is to apply predictive engineering methods, which enable the evaluation of various design alternatives already at the early design stages. The main numerical prediction tools for evaluating low-frequency (vibro-) acoustic product performance are based on the finite element (FE) and the boundary element (BE) method.

The *finite element* (FE) *method* is the most commonly used method for solving dynamic problems, defined in bounded continuum domains. For a time-harmonic sound field, for instance, the steady-state pressure field $p(r,\omega)$ is governed by the Helmholtz equation

$$\nabla^2 p(\mathbf{r},\omega) + k^2 \cdot p(\mathbf{r},\omega) = -\mathrm{j}\rho\omega q, \tag{3}$$

where ∇^2 is the Laplace operator, $k=\omega/c$ is the acoustic wavenumber, ω is the angular frequency, c is the speed of sound in the fluid, ρ is the ambient fluid density, q is a volume velocity source distribution, $\mathbf{r}$ is a position vector and $\mathrm{j}=\sqrt{-1}$.

The FE calculation of such a pressure field in a bounded cavity is based on the discretization of the cavity volume into small elements and the definition of nodes at some discrete locations in each element. Within each element, the pressure field is approximated in terms of simple prescribed shape functions N_a, which are locally defined within the element,

$$p(\mathbf{r},\omega) \approx \sum N_a(\mathbf{r}) \cdot p_a(\omega) = \mathbf{N}_a \cdot \mathbf{p}_a. \tag{4}$$

The element shape functions are defined such that the vector of unknown shape function contributions $\mathbf{p}_a$ consists of the pressure approximations at the nodal locations. By transforming the Helmholtz equation (3) into a weighted residual or a variational formulation and by taking into account the boundary conditions, a matrix equation in the unknown nodal pressures is obtained [3–5],

$$(\mathbf{K}_a + \mathrm{j}\omega\mathbf{C}_a - \omega^2\mathbf{M}_a) \cdot \mathbf{p}_a = \mathbf{F}_a. \tag{5}$$

The acoustic stiffness and mass matrices $\mathbf{K}_a$ and $\mathbf{M}_a$ are sparsely populated, symmetric matrices with real, frequency-independent coefficients, while the sparsely populated, symmetric damping matrix $\mathbf{C}_a$ has usually complex, frequency-dependent coefficients.

The *boundary element* (BE) *method* is a commonly used alternative for solving acoustic problems, especially for predicting the steady-state pressure field in unbounded fluid domains. The method is based on a boundary integral formulation, which relates the steady-state pressure at any position in the fluid domain to the distributions of two acoustic variables on the boundary surface of the considered problem. In this way, the BE method follows a two-step procedure. In the first step, the distributions of the boundary surface variables are determined. In the second step, the steady-state pressure at any position in the (unbounded) fluid domain can be obtained from the boundary integral formulation, using the boundary surface results from the first step.

For inhomogeneous acoustic problems, i.e., when a non-zero volume velocity source distribution q is applied (3), the total pressure field p may be regarded as a superposition of a homogeneous pressure field p_a and an inhomogeneous free-field pressure p_b,

$$p = p_a + p_b. \tag{6}$$

The pressure field p_b represents the free-field pressure due to the volume velocity source distribution q,

$$\nabla^2 p_b(\mathbf{r},\omega) + k^2 \cdot p_b(\mathbf{r},\omega) = -\mathrm{j}\rho\omega q. \tag{7}$$

An analytical solution for this pressure field p_b may be obtained, since the source distribution q can be regarded as a combination of acoustic point sources. For a single point source with a volume velocity Q, located at position $\mathbf{r}_q$, i.e., $q = Q \cdot \delta(\mathbf{r},\mathbf{r}_q)$, where δ is a Dirac delta function, the free-field pressure is

$$p_b = -\mathrm{j}\rho\omega Q \cdot G(\mathbf{r},\mathbf{r}_q,\omega) = -\mathrm{j}\rho\omega Q \cdot \frac{\mathrm{e}^{-\mathrm{j}k\|\mathbf{r}-\mathbf{r}_q\|}}{4\pi\|\mathbf{r}-\mathbf{r}_q\|}, \tag{8}$$

where G is the Green kernel function. In some commercially available software packages for (vibro-) acoustic simulations, as e.g. in LMS/SYSNOISE, an acoustic point source is characterized by its source strength A, which is the pressure in free-field conditions at a distance of 1 m from the source position. It follows from Eq. (8) that there is a relation between the (complex) source strength A and its corresponding volume velocity Q, i.e.,

$$A = \frac{-\mathrm{j}\rho\omega Q}{4\pi}. \tag{9}$$

It is important to point out that, even though a fixed free-field volume velocity Q is applied via the fixed source strength A, the resulting volume velocity of the source will also depend on the acoustic impedance of the environment in which the source is located. A detailed discussion of this phenomenon is given in Section 5.

The homogeneous pressure field p_a is defined as the solution of the homogeneous Helmholtz equation

$$\nabla^2 p_a(\mathbf{r},\omega) + k^2 \cdot p_a(\mathbf{r},\omega) = 0. \tag{10}$$

The boundary conditions for this homogeneous pressure field result from a reformulation of the boundary conditions of the original acoustic problem. As a result of the above described pressure decomposition (6) of the pressure field p, a numerical solution procedure is needed only for the homogeneous subproblem. Therefore, the discussion of the indirect BE method below will be confined to homogeneous acoustic problems without loss of generality.

The indirect BE method is commonly used for predicting the steady-state pressure field, radiated from a thin-walled (open or closed) vibrating surface. The method is based on the indirect boundary integral formulation [6], which relates the pressure at any position $\mathbf{r}$ in an (unbounded) fluid domain that surrounds the vibrating structure, having a boundary surface S, to the distributions of a single layer potential $\sigma(\mathbf{r}_a, \omega)$ and a double layer potential $\mu(\mathbf{r}_a, \omega)$ on that boundary surface,

$$p(\mathbf{r}, \omega) = \int_S \left[\mu(\mathbf{r}_a, \omega) \cdot \frac{\partial G(\mathbf{r}, \mathbf{r}_a, \omega)}{\partial n} - \sigma(\mathbf{r}_a, \omega) \cdot G(\mathbf{r}, \mathbf{r}_a, \omega) \right] \mathrm{d}S(\mathbf{r}_a). \tag{11}$$

The single layer potential σ is the difference in normal pressure gradient between both sides of the thin boundary surface and the double layer potential μ is the pressure difference between both sides,

$$\sigma(\mathbf{r}_a, \omega) = \frac{\partial p(\mathbf{r}_a^+, \omega)}{\partial n} - \frac{\partial p(\mathbf{r}_a^-, \omega)}{\partial n}, \tag{12}$$

$$\mu(\mathbf{r}_a, \omega) = p(\mathbf{r}_a^+, \omega) - p(\mathbf{r}_a^-, \omega). \tag{13}$$

The positions $\mathbf{r}_a^+$ and $\mathbf{r}_a^-$ indicate the boundary surface positions at the positive and negative side of the normal direction n.

In a similar way as is done in the FE method, the indirect BE method is based on the discretization of the boundary surface S into small elements and the single and double layer potentials are approximated in terms of locally defined element shape functions. In many practical applications, the single layer potential is either zero or related to the double layer potential through an impedance boundary condition. In such cases, the double layer potential is the only independent boundary surface variable, which is approximated as

$$\mu(\mathbf{r}_a, \omega) \approx \sum N_\mu(\mathbf{r}_a) \cdot \mu_a(\omega) = \mathbf{N}_\mu \cdot \boldsymbol{\mu}_a. \tag{14}$$

Transforming the indirect boundary integral formulation (11), together with the boundary conditions of the considered problem, into a variational formulation and imposing the stationarity condition on the associated energy functional yields a matrix equation in the unknown nodal double layer potentials [7],

$$\mathbf{H}(\omega) \cdot \boldsymbol{\mu}_a = \mathbf{F}_\mu. \tag{15}$$

Model matrix $\mathbf{H}$ is symmetric, but, in contrast with an FE model, it is fully populated with complex, frequency-dependent coefficients which result from more complicated numerical integrations than it is the case for FE model coefficients. Moreover, for exterior radiation problems with a closed boundary surface, the boundary integral formulation suffers from non-uniqueness of the solution at some particular (irregular) frequencies, which requires special numerical treatment to circumvent this problem [8].

Compared with an FE model, the size of a BE model is significantly smaller, since only the problem boundary surface must be discretized into elements. However, the smaller model size usually does not result in smaller computational efforts. A small, but fully populated and frequency-dependent BE model must be constructed and solved at each frequency of interest. The construction of an FE model, however, is computationally efficient, since it usually involves only an assembly of frequency-independent submatrices. Moreover, efficient matrix solvers are available for large, but sparsely populated, symmetric FE models. As a result, the FE method is usually computationally more efficient for solving acoustic problems, defined in a bounded fluid domain, while the strength of the BE method becomes mainly apparent for solving radiation problems in unbounded fluid domains.

In the FE and the BE method, the dynamic variables within each element are expressed in terms of simple (polynomial) shape functions. In order to represent the spatial variation of the dynamic response accurately within each element, a substantial number of elements is required. In this respect, a rule of thumb states that at least 10 (linear) elements per wavelength are needed. This may result in large models, whose size increases for increasing frequency, since the acoustic wavelength $\lambda = 2\pi/k = 2\pi c/\omega$ decreases for increasing frequency. Since the subsequent computational efforts increase also, the use of FE and BE methods is practically restricted to the low-frequency range.

4.2. Numerical modelling approaches

For the numerical prediction of the low-frequency insertion loss of a driver's cabin, three different modelling approaches are presented. Both the direct and the reciprocal *IL* definition are used in order to assess the impedance effect of the environment onto the source volume velocity. In the description of the numerical approaches, only the calculation of p_{cabin} is taken into account, since p_{source} can be calculated analytically by using the free-field pressure expression (8).

4.2.1. Fully coupled approach

In principle, the mutual fluid–structure coupling interaction between the cabin structural vibrations and the acoustic pressures in both the cabin interior fluid and the exterior fluid must be taken into account. For this purpose, a structural FE model for the cabin vibrations can be coupled with an acoustic BE model of type (15) for the interior and exterior pressure fields,

$$\begin{bmatrix} (\mathbf{K}_s + \mathrm{j}\omega\mathbf{C}_s - \omega^2\mathbf{M}_s) & \mathbf{L}_c \\ \mathbf{L}_c^{\mathrm{T}} & \dfrac{\mathbf{H}(\omega)}{\rho\omega^2} \end{bmatrix} \cdot \begin{Bmatrix} \mathbf{w}_s \\ \boldsymbol{\mu}_a \end{Bmatrix} = \begin{Bmatrix} \mathbf{F}_s \\ \mathbf{F}_\mu \end{Bmatrix} \tag{16}$$

$\mathbf{K}_s$, $\mathbf{C}_s$ and $\mathbf{M}_s$ are the structural stiffness, damping and mass matrices, $\mathbf{w}_s$ is the vector of unknown nodal displacement degrees of freedom of the cabin structure [9]. The coupling matrix $\mathbf{L}_c$ results from the pressure loading effect of the interior and exterior sound fields on the cabin structural displacements, while the transpose of the coupling matrix arises in the acoustic part of the coupled model (16) to ensure that the normal fluid displacements along the fluid–structure interface equal the normal structural displacements. The coupled FE/BE model (16) can be directly solved at each frequency of interest for the unknown nodal structural displacements and acoustic double layer potentials. The latter potentials then allow the calculation of the pressure at any field point in the fluid domains using the boundary integral formulation (11).

Especially for low-frequency predictions, the size of the coupled model (16) can be reduced without substantial loss of accuracy by projecting the structural displacements onto a modal base of in-vacuo normal modes,

$$\mathbf{w}_s = \boldsymbol{\Phi}_s \cdot \boldsymbol{\phi}_s. \tag{17}$$

The columns of matrix $\mathbf{\Phi}_s$ are normalized modes and vector $\boldsymbol{\phi}_s$ comprises their contribution factors to the structural displacement. The resulting coupled model then becomes

$$\begin{bmatrix} (\tilde{\mathbf{K}}_s + \mathrm{j}\omega\tilde{\mathbf{C}}_s - \omega^2\mathbf{I}_s) & \mathbf{\Phi}_s^{\mathrm{T}}\mathbf{L}_c \\ \mathbf{L}_c^{\mathrm{T}}\mathbf{\Phi}_s & \dfrac{\mathbf{H}(\omega)}{\rho\omega^2} \end{bmatrix} \cdot \begin{Bmatrix} \boldsymbol{\phi}_s \\ \boldsymbol{\mu}_a \end{Bmatrix} = \begin{Bmatrix} \mathbf{\Phi}_s^{\mathrm{T}}\mathbf{F}_s \\ \mathbf{F}_\mu \end{Bmatrix} \tag{18}$$

$\tilde{\mathbf{K}}_s$ is a diagonal matrix, containing the squared natural frequencies ω_s^2 of the considered modes. The modal damping matrix $\tilde{\mathbf{C}}_s$ is usually constructed as a diagonal matrix with coefficients either of type $2\xi_s\omega_s$, in which ξ_s represents a modal viscous damping coefficient, or of type $\eta_s\omega_s^2/\omega$, in which η_s represents a modal hysteretic damping coefficient.

The *direct IL* can be determined by calculating the pressure inside the cabin, due to an acoustic source excitation outside. The *reciprocal IL* is determined by calculating the pressure response outside the cabin, due to an acoustic excitation inside. In both procedures, the same type of fully coupled numerical model is used.

Since a structural and an acoustic problem must be solved simultaneously, the size of a coupled FE/BE model (16), even in its semi-modal form (18), becomes very large. For this reason and due to the frequency dependence of the acoustic part of the model, the computational efforts, involved with solving a fully coupled model for a real-life driver's cabin in a wide frequency range, become prohibitively large, even with the nowadays available powerful computer resources.

4.2.2. Semi-coupled approach

Although the cabin structural vibrations mutually interact with both the interior and the exterior pressure fields, the strength of the fluid–structure coupling interaction between the cabin vibrations and the interior pressure is significantly larger, since the cabin interior is a closed fluid cavity with a relatively small volume. Therefore, a two-step semi-coupled modelling approach can be followed, in which the mutual coupling interaction between the cabin vibrations and the exterior pressure field is neglected. This approach is computationally more efficient than the fully coupled approach, however at the expense of some accuracy loss. A distinction has to be made between the semi-coupled modelling procedure for the *direct* and for the *reciprocal IL* calculations.

In the *first step* of the *direct IL* calculation, the blocked pressure response, due to an acoustic source outside the cabin is calculated using a BE model of type (15). The blocked pressure represents the pressure on the cabin outer surface, when this surface is assumed to be rigid. This blocked pressure distribution is then translated into a normal force distribution, which is used as excitation for the structural FE model in the second step. In the *second step* of the *direct IL* calculation, the coupled dynamic response of the cabin structure and the interior fluid due to a distributed structural force excitation is calculated, while the effect of the exterior pressure field is disregarded. For this purpose, a structural FE model for the cabin vibrations can be coupled with an acoustic FE model of type (5) for the cabin interior pressure field [4]

$$\begin{bmatrix} (\mathbf{K}_s + \mathrm{j}\omega\mathbf{C}_s - \omega^2\mathbf{M}_s) & \mathbf{K}_c \\ \rho\omega^2\mathbf{K}_c^{\mathrm{T}} & (\mathbf{K}_a + \mathrm{j}\omega\mathbf{C}_a - \omega^2\mathbf{M}_a) \end{bmatrix} \cdot \begin{Bmatrix} \mathbf{w}_s \\ \mathbf{p}_a \end{Bmatrix} = \begin{Bmatrix} \mathbf{F}_s \\ \mathbf{F}_a \end{Bmatrix}. \tag{19}$$

The coupling matrix $\mathbf{K}_c$ results from the pressure loading effect of the interior sound field on the cabin structural displacements, while the coupling matrix $\rho\omega^2\mathbf{K}_c^{\mathrm{T}}$ arises in the acoustic part of the coupled model (19) to ensure that the normal fluid displacements along the fluid–structure interface equal the normal structural displacements.

Again, a modal expansion may reduce the size of the coupled model (19). The most appropriate modal base consists of the modes of the coupled system. However, since the coupled model (19) is not symmetric, the calculation of coupled modes requires a non-symmetric eigenvalue calculation, which is very time consuming and which makes it a practically impossible procedure for many real-life vibro-acoustic problems. A possible alternative is to apply a component mode synthesis technique. The structural displacements can be projected onto a base of uncoupled structural modes, i.e., modes of the structure without fluid pressure loading (see Eq. (17)). The fluid pressures can be projected onto a base of uncoupled acoustic modes $\mathbf{\Phi}_a$, i.e., acoustic modes with rigid boundary conditions along the fluid–structure interface,

$$\mathbf{p}_a = \mathbf{\Phi}_a \cdot \boldsymbol{\phi}_a. \tag{20}$$

The resulting coupled model then becomes

$$\begin{bmatrix} (\tilde{\mathbf{K}}_s + \mathrm{j}\omega\tilde{\mathbf{C}}_s - \omega^2\mathbf{I}_s) & \mathbf{\Phi}_s^{\mathrm{T}}\mathbf{K}_c\mathbf{\Phi}_a \\ \rho\omega^2\mathbf{\Phi}_a^{\mathrm{T}}\mathbf{K}_c^{\mathrm{T}}\mathbf{\Phi}_s & (\tilde{\mathbf{K}}_a + \mathrm{j}\omega\tilde{\mathbf{C}}_a - \omega^2\mathbf{I}_\mathbf{a}) \end{bmatrix} \cdot \begin{Bmatrix} \boldsymbol{\phi}_s \\ \boldsymbol{\phi}_a \end{Bmatrix} = \begin{Bmatrix} \mathbf{\Phi}_s^{\mathrm{T}}\mathbf{F}_s \\ \mathbf{\Phi}_a^{\mathrm{T}}\mathbf{F}_a \end{Bmatrix}. \tag{21}$$

The advantage of using uncoupled modes is that these modes result from symmetric and computationally efficient eigenvalue problems. It should be noted, however, that uncoupled acoustic modes have a zero fluid displacement component, normal to the fluid–structure coupling interface, which implies that a large number of high-order uncoupled acoustic modes is required to accurately represent the normal displacement continuity along the fluid–structure interface. By solving the coupled system (21), p_{cabin} can be calculated.

In the *first step* of the *reciprocal IL* calculation, the coupled dynamic response of the cabin structure and the interior fluid, due to an acoustic source excitation in the cabin interior is calculated, while the effect of the exterior pressure field is disregarded. For this purpose, a structural FE model for the cabin vibrations can be coupled with an acoustic FE model of type (5) for the cabin interior pressure field. Again, like in step 2 of the *direct* procedure, a modal expansion may reduce the size of the coupled model (19). In the *second step* of the *reciprocal IL* calculation, the exterior pressure is calculated using a BE model of type (15). The mesh of the BE model consists of the exterior envelope of the structural FE mesh. The normal structural velocities on this envelope are extracted from the results, obtained from the first step. These structural velocities, which serve as normal velocity boundary conditions for the exterior radiation problem, are then used to construct the excitation vector $\mathbf{F}_\mu$ of the BE model (15). Finally, the resulting double layer potentials on the BE mesh are used to calculate the pressure p_{cabin}.

4.2.3. Uncoupled approach

By neglecting the mutual coupling interaction of the cabin structural vibrations with both the interior and the exterior pressure fields, a three-step uncoupled modelling approach is obtained, which is the computationally most efficient, but least accurate approach.

The *first step* of the *direct IL* calculation is completely similar to the first step of the semi-coupled approach, in that the blocked pressure on the structure, due to an acoustic source excitation outside the cabin, is calculated with a BE model. In the *second step* of the *direct IL* calculation, the cabin structural displacements are calculated from an uncoupled structural FE model, in which the pressures at the fluid–structure interface, obtained in the first step, are used as external force excitations. In the *third step* of the *direct IL* calculation, an uncoupled acoustic FE model of type (5), in which the cabin structural vibrations from the second step are used as normal velocity inputs, is used to calculate the cabin interior pressure field.

In the *first step* of the *reciprocal IL* calculation, an uncoupled acoustic FE model of type (5) is used to calculate the cabin interior pressure field due to an acoustic source excitation. For this pressure calculation, the cabin structure is assumed to be rigid. In the *second step* of the *reciprocal IL* calculation, the cabin structural displacements are calculated from an uncoupled structural FE model, in which the pressures at the fluid–structure interface, obtained in the first step, are used as external force excitations. The *third step* of the *reciprocal IL* calculation is completely similar to the second step of the semi-coupled approach, in that the exterior pressure is obtained from an acoustic BE model, in which the cabin structural vibrations from the second step are used as normal velocity inputs. By applying the double layer potentials in the boundary integral formulation (11), p_{cabin} is obtained.

Note that for all the uncoupled structural and acoustic FE calculations, a modal projection of types (17) and (20), respectively, can be used to reduce the model size.

5. Cabin scale model validations

5.1. Preliminary considerations

As described in Section 2, the cabin scale model is placed on a rubber mat, which rests on the rigid floor of a semi-anechoic test room. Although the rubber mat has a finite normal impedance, it is assumed in the numerical modelling that the rubber mat is rigid, having an infinitely large normal impedance, which is a fair assumption at low frequencies.

To account for the effect of the rigid floor in the numerical calculation of the low-frequency pressure *IL* of the cabin scale model, the pressure p_{source} at position $\mathbf{r}$ in the half-space due to a time-harmonic point source excitation at position $\mathbf{r}_q$ with frequency ω is obtained from a modified Green function where G_H [10]

$$G_H(\mathbf{r}, \mathbf{r}_a, \omega) = \frac{e^{-jkR_1}}{4\pi R_1} + \frac{e^{-jkR_2}}{4\pi R_2} \tag{22}$$

with $R_1 = \|\mathbf{r} - \mathbf{r}_q\|$ the distance between the source position $\mathbf{r}_q$ and position $\mathbf{r}$ and with $R_2 = \|\mathbf{r}' - \mathbf{r}_q\|$ the distance between the source position and position $\mathbf{r}'$, being the mirror position of $\mathbf{r}$ with respect to the rigid floor (see Fig. 11).

5.2. Numerical models

For the calculation of the structural vibrations, the panels of the cabin scale model have been discretized into four-noded third order plate elements, yielding a structural FE mesh with a total of 22 991 unconstrained degrees of freedom. The wavelength of bending waves in flat

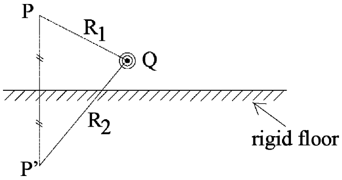

Fig. 11. The effect of the rigid floor on the free-field pressure response of an acoustic point source.

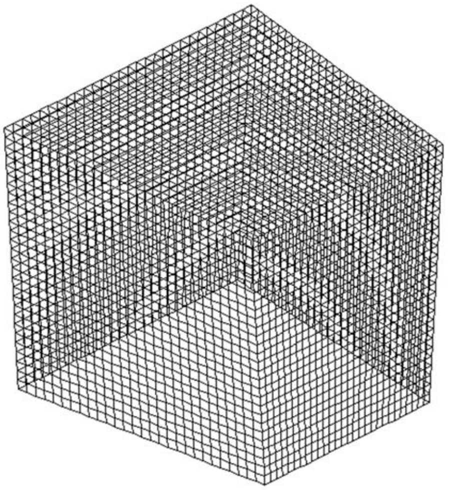

Fig. 12. Scale model structural FE mesh.

panels equals

$$\lambda_b = \sqrt[4]{\frac{4\pi^4 E t^2}{3\rho_s \omega^2 (1 - v^2)}} \tag{23}$$

with t the panel thickness, E the modulus of elasticity, ρ_s the plate density and v the Poisson ratio. Based on the panel properties in Table 1 and a rule of thumb that states that at least five third-order plate elements are needed per wavelength, the structural FE mesh, shown in Fig. 12, may provide accurate displacement predictions up to 350 Hz.

In all calculations, a modal projection of type (17) is used for the structural displacements. The modal base contains 331 modes, which constitute all the in-vacuo modes of the scale model structure with natural frequencies ω_s less than 400 Hz. For each of these modes, a modal hysteretic damping η_s of 0.03 is defined.

The acoustic part of the fully coupled model (18) is based on a BE mesh of four-noded linear fluid elements. Since low-frequency acoustic wavelengths are much larger than structural bending wavelengths, acoustic meshes could be coarser than structural meshes. However, it is advisable for coupled vibro-acoustic predictions to use an acoustic mesh with a similar mesh density as the corresponding structural FE mesh in order to allow an accurate modelling of the continuity of the normal fluid and structural displacements along the fluid–structure coupling interface. Therefore, the nodes of the acoustic BE mesh coincide with the nodes of the FE mesh of the scale model structure, yielding a total of 3923 acoustic degrees of freedom. Note that the rigid floor of the semi-anechoic testroom is not explicitly included in the BE mesh. By using function G_H, defined in Eq. (22), as the Green kernel function in the boundary integral formulation (11), the effect of the rigid floor is implicitly taken into account in the BE model and the surface integral in Eq. (11) must only be evaluated along the surface of the scale model.

In the semi-coupled and uncoupled modelling approaches, the calculation of the pressure field in the interior cavity is based on an acoustic FE mesh of eight-noded linear volume elements. Again, a similar mesh density is adopted as in the structural FE mesh, yielding a volume mesh with a total of 24 389 nodal pressure degrees of freedom. In the calculations, the nodal pressures are projected onto a modal base of type (20). The base contains 40 acoustic modes, which constitute all uncoupled cavity modes with natural frequencies ω_a less than 780 Hz. Note that this frequency span of the acoustic modal base is larger than the 400 Hz frequency span of the structural modal base. As mentioned before, higher-order uncoupled acoustic modes are taken into account to accurately represent the normal displacement continuity along the interface between the scale model structure and the interior cavity.

In all acoustic models, the air is modelled with a speed of sound $c = 340\,\mathrm{m/s}$ and a mass density $\rho = 1.2\,\mathrm{kg/m^3}$.

5.3. Source modelling

As mentioned in Sections 3 and 4, the modelling of the acoustic source is a crucial point in calculating the *IL*. To be able to apply the reciprocal definition, the acoustic source must have a volume velocity which is independent of the acoustic impedance of the environment that surrounds the source.

One way to guarantee this independence is to apply a fixed volume velocity for all frequencies. To obtain this, the source can be modelled as a small surface on which normal velocity boundary conditions v are applied in such a way that the surface acts as a pulsating panel (see Fig. 13). The dimensions of the surface should be small compared to the acoustic wavelengths. In this case, a panel edge length has been used, which is less than 1/40 of the acoustic wavelengths at 350 Hz, being the highest frequency of interest. In this way, the vibrating panel surface (with area S) can be considered as a point source with volume velocity,

$$Q = 2Sv. \tag{24}$$

As indicated in Section 4.1, another way to characterize an acoustic source, is through its source strength A, being linked with its free-field volume velocity Q (see Eq. (9)). However, the resulting

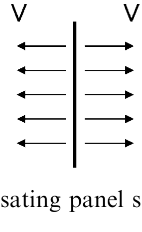

Fig. 13. Pulsating panel source model.

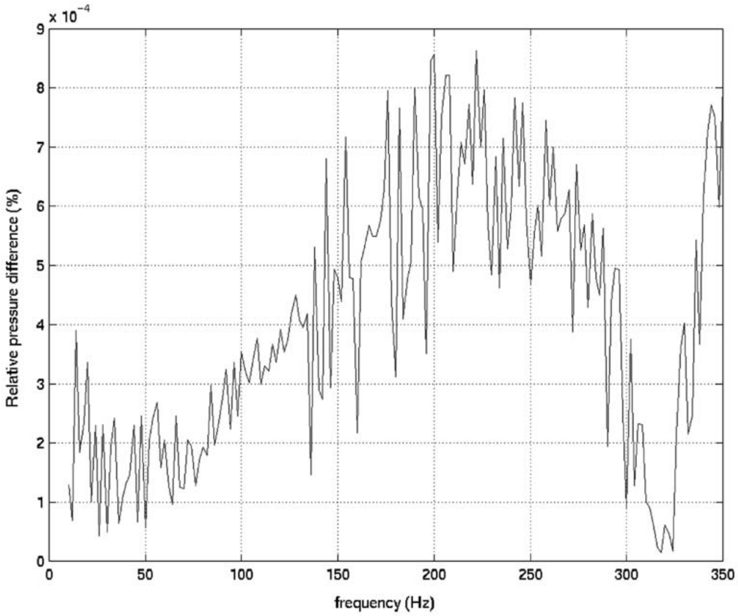

Fig. 14. The relative difference (in %) in the pressure responses in a point in a half-space due to the pulsating panel excitation and due to a source with free-field source strength characterization.

volume velocity using this source characterization type is dependent on the impedance 'seen' by the source.

Fig. 14 shows the relative difference (in %) in the pressure responses in a point in a free half-space (see Fig. 11), obtained with the two source characterisations. Since the difference is very small, it may be concluded that, at low frequencies, the pulsating panel source is a good approximation of a point source.

5.4. *Discussion of results*

The three modelling approaches have been used to evaluate the airborne insertion loss of the scale model using both source characterization methods, in the range from 10 to 350 Hz with a frequency step of 2 Hz. The uncoupled structural results are obtained with the MSC/NASTRAN v70.7 software, while the acoustic and coupled vibro-acoustic results are obtained with the LMS/SYSNOISE Rev. 5.5 software. All calculations have been performed on an HP-C3000 Unix-workstation (400 MHz single processor, 2.5 Gb memory, SPECint95 = 31.8, SPECfp95 = 52.4).

5.4.1. *Fully coupled approach*

Fig. 15 shows the *direct* and the *reciprocal IL* calculation using a pulsating panel source. Both curves are almost identical, which indicates that this method to characterize an acoustic source is independent of its impedance environment. There is, however, a very small difference between the two curves. Fig. 16 shows the difference in p_{cabin} when the pulsating panel is located out- and

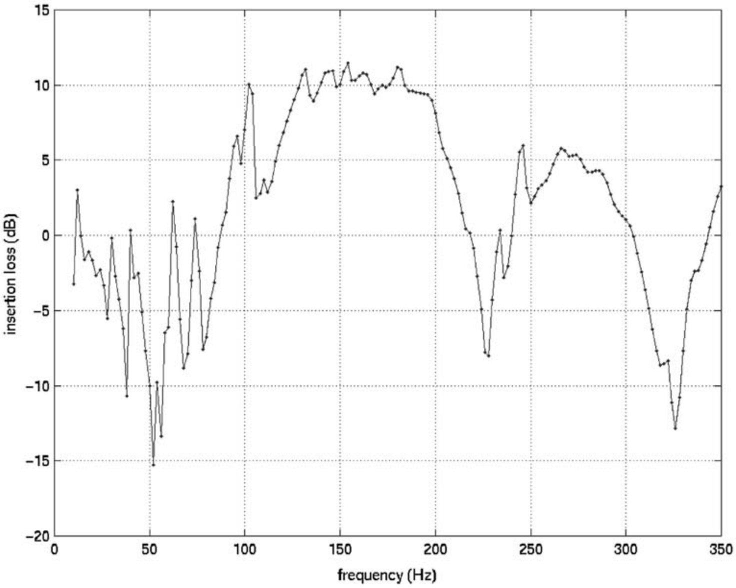

Fig. 15. Direct *IL* (solid line) and reciprocal *IL* (dotted line) of the cabin scale model calculated with the fully coupled approach using a pulsating panel source.

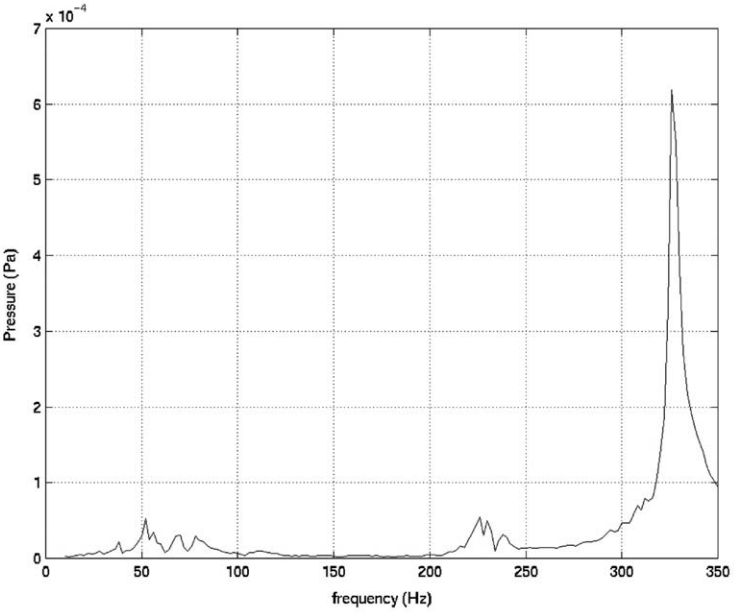

Fig. 16. Pressure difference in the fully coupled approach using a pulsating panel source, caused by the change in impedance.

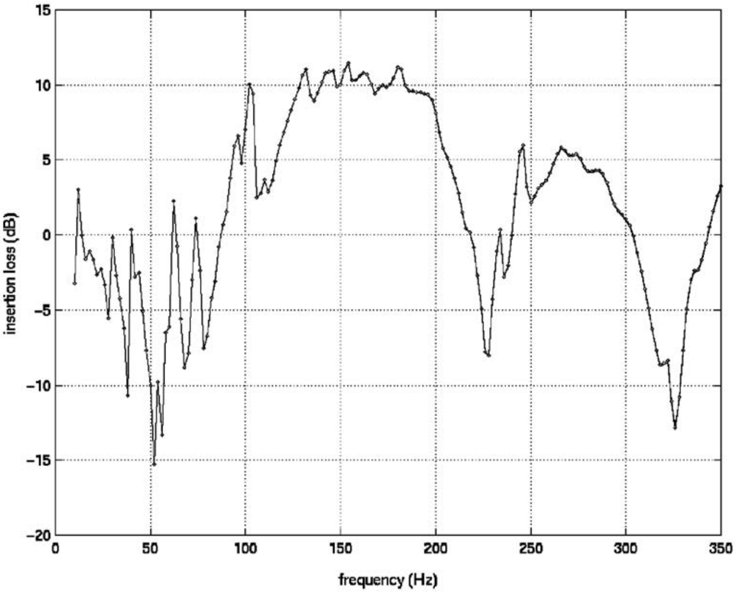

Fig. 17. Direct *IL* (solid line) and reciprocal *IL* (dotted line) of the cabin scale model calculated with the fully coupled approach using a free-field source strength characterization.

inside the cabin scale model. Only at the acoustic resonances (see Table 3) some very small differences can be noticed.

Fig. 17 shows the *direct* and the *reciprocal IL* determined by using the free-field source strength modelling method. Again both curves are almost identical. Fig. 18 shows the difference in p_{cabin} when the point source is located out- and inside the cabin scale model (solid line) together with the results of the pulsating panel method (dotted line). This figure clearly shows that the free-field source strength modelling method is much more dependent on the source environment than the pulsating panel method. This behaviour, again, is most apparent at the acoustic resonance frequencies of the cabin. It is also at these resonance frequencies that the *IL* is becoming negative (see Figs. 15 and 17). This indicates poor insulation behaviour and is caused by the high vibration levels of the scale model structure, due to the large acoustic response inside the scale model cavity at resonance.

Note that the small differences between both curves in Fig. 17 indicate that, for the considered case, no significant changes occur in the impedance 'seen' by the source.

5.4.2. Semi-coupled approach

Figs. 19 and 20 show, respectively, the *IL* results for the pulsating panel and for the free-field source strength method. The solid line represents the *direct IL* and the dotted line the *reciprocal IL*. Fig. 21 shows the difference in p_{cabin} between the *direct* and the *reciprocal* approach, for both source characterisation techniques. It is clear that the free-field source strength method is more sensitive to changing the environment of the source from a free half-space to a closed cavity and to neglecting the exterior coupling.

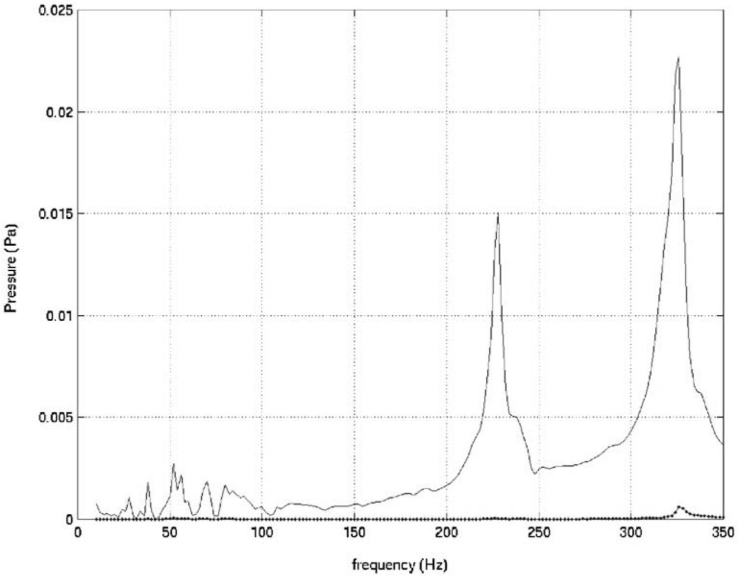

Fig. 18. Pressure difference in the fully coupled approach caused by the change in impedance (dotted line: pulsating panel source; solid line: free-field source strength characterization).

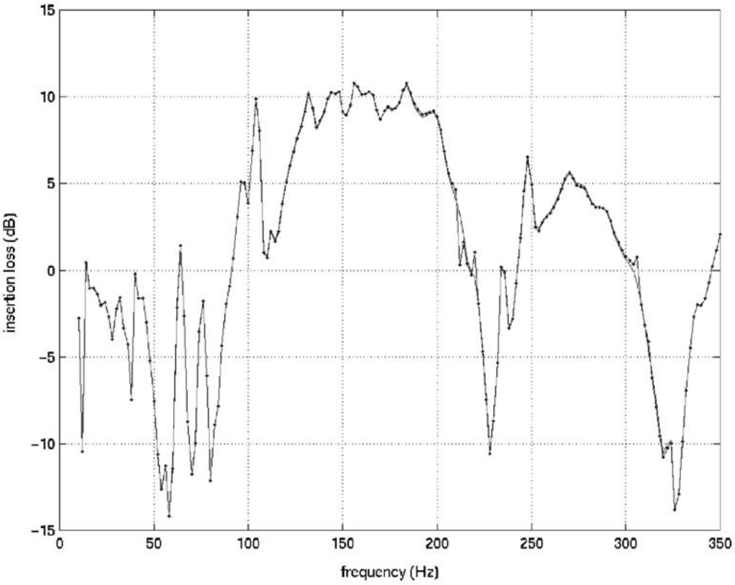

Fig. 19. Direct *IL* (solid line) and reciprocal *IL* (dotted line) of the cabin scale model calculated with the semi-coupled approach using a pulsating panel source.

5.4.3. Uncoupled approach

Figs. 22 and 23 show, respectively, the *IL* results for the pulsating panel and for the free-field source strength method. The solid line represents the *direct IL* and the dotted line

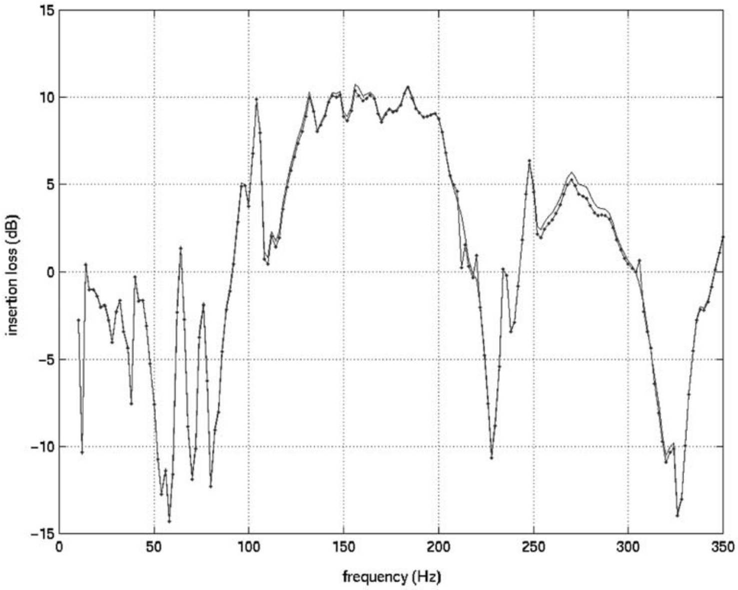

Fig. 20. Direct *IL* (solid line) and reciprocal *IL* (dotted line) of the cabin scale model calculated with the semi-coupled approach using a free-field source strength characterization.

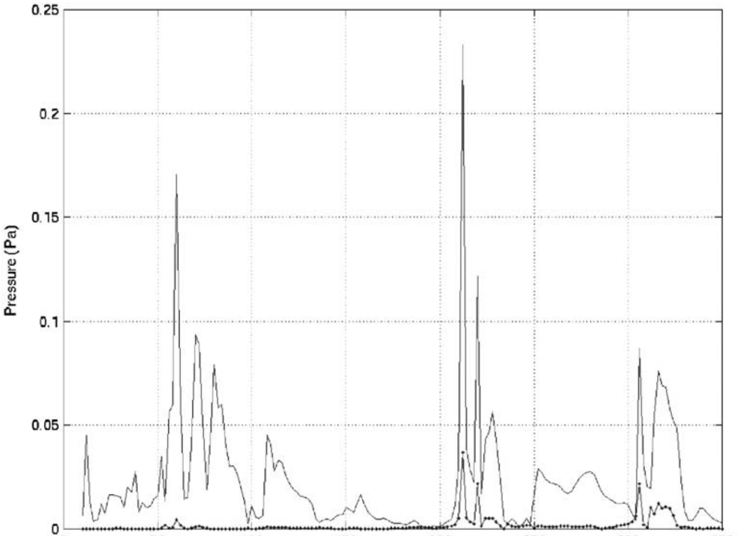

Fig. 21. Pressure difference in the semi-coupled approach caused by the change in impedance (dotted line: pulsating panel source; solid line: free-field source strength characterization).

the *reciprocal IL*. These figures indicate that by neglecting the vibro-acoustic coupling between the cabin and the interior air, the reciprocity is still accurately represented. Fig. 24 shows the difference in p_{cabin} between the *direct* and the *reciprocal* approach, for both source

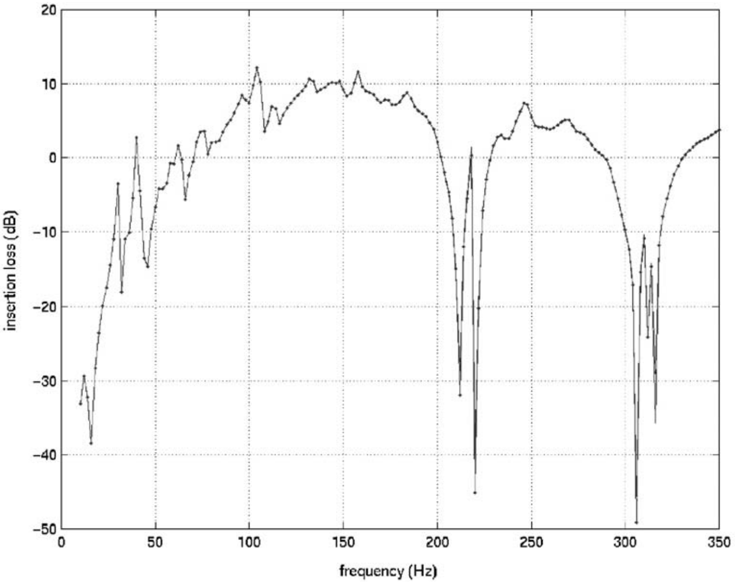

Fig. 22. Direct *IL* (solid line) and reciprocal *IL* (dotted line) of the cabin scale model calculated with the uncoupled approach using a pulsating panel source.

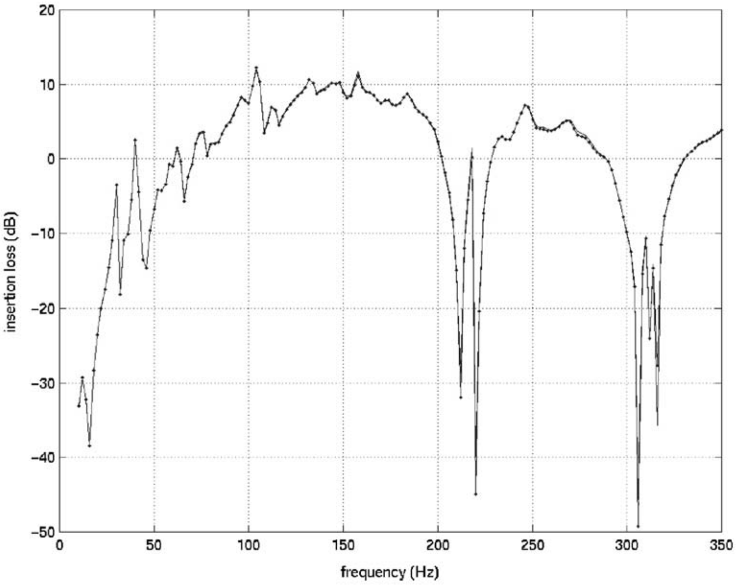

Fig. 23. Direct *IL* (solid line) and reciprocal *IL* (dotted line) of the cabin scale model calculated with the uncoupled approach using a free-field source strength characterization.

modelling methods. Again the free-field source strength method is most sensitive for changes in the impedance ‘seen’ by the source and for neglecting all vibro-acoustic coupling effects.

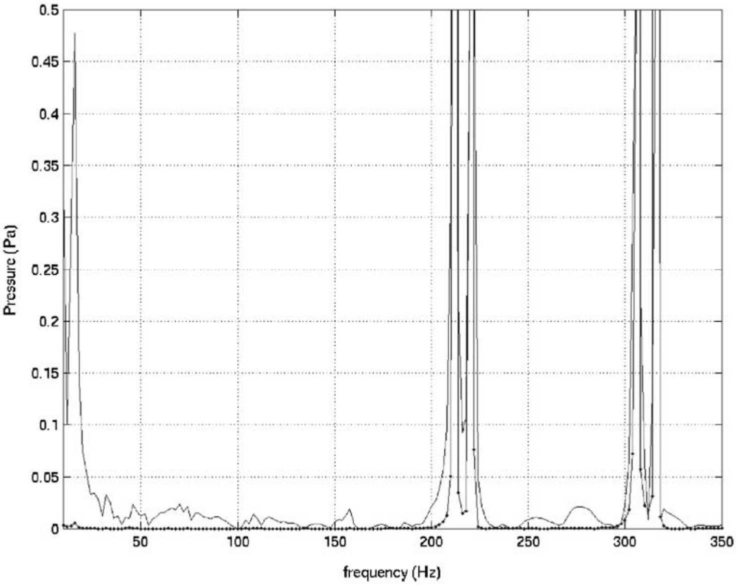

Fig. 24. Pressure difference in the uncoupled approach caused by the change in impedance (dotted line: pulsating panel source; solid line: free-field source strength characterization).

5.4.4. Conclusions

In all three approaches, it is clear that the pulsating panel source modelling method performs better than the free-field source strength method. However, the latter is easier to implement, since no source panel surface should be included in the FE and BE meshes, while still providing good accuracy.

Fig. 25 compares the *reciprocal IL* with the free-field source strength method, obtained with all three approaches. The uncoupled approach is clearly not very accurate, while the semi-coupled and the fully coupled approach give similar results. This indicates that the assumption that the vibro-acoustic coupling between the scale model and the interior air is more important than the coupling with the exterior air, is justified. The coupling with the exterior air may even be neglected, without loosing much accuracy in determining the *IL*.

Fig. 26 compares the measured reciprocal power insertion loss of the cabin scale model with the numerical results, obtained with the three modelling approaches, using the free-field source strength method. The reciprocal power insertion loss is the logarithmic ratio between the total power radiated by the sound source in free-field conditions and the total power radiated by the scale model, being excited by the source inside the cavity. The most commonly used sound power measurement procedure utilises a two-microphone sound intensity probe [11–13]. The acoustic intensity is integrated over a surface and can experimentally be approximated either by measuring the intensity at some discrete points [14] or by scanning [15]. Fig. 26 illustrates that the fully coupled modelling approach provides accurate prediction results in the frequency range below 350 Hz. As could be expected, the accuracy drops above this frequency, since the frequency span of the structural modal base is limited to 400 Hz and since the structural FE mesh becomes too coarse for higher frequencies. It can be noticed that the numerically identified frequencies of poor

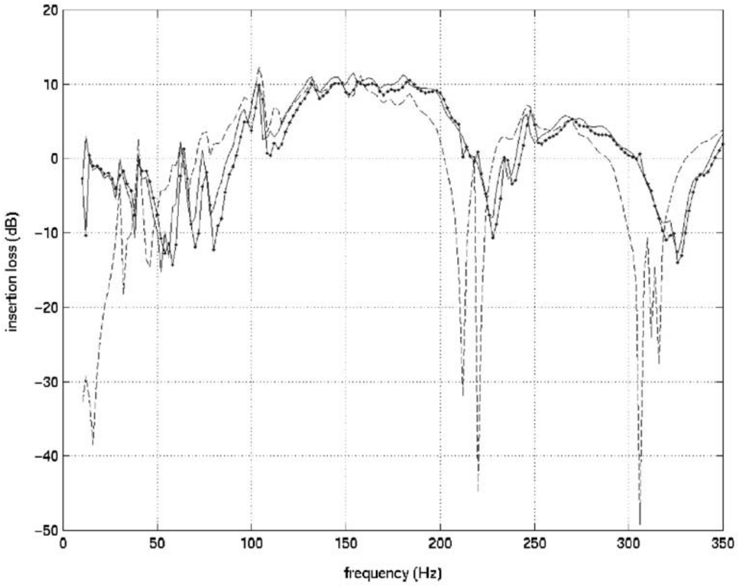

Fig. 25. Reciprocal *IL* with the free-field source strength characterization (full line: fully coupled; dotted line: semi-coupled; dashed line: uncoupled).

insulation (e.g., around 235 and 330 Hz) are slightly smaller than the measured frequencies. This may be due to small errors on the air density and speed of sound and due to small geometrical errors. The latter is caused by the fact that the boundary surface of the cavity volume in the numerical models coincides with the middle surfaces of the panels, whereas the actual cavity dimensions are slightly smaller due to the finite thickness of the panels. Compared with the fully coupled approach, the accuracy of the semi-coupled approach is slightly smaller, but still reasonable in the frequency range below 350 Hz, whereas the accuracy of the uncoupled approach is fairly poor.

5.5. *Computational efficiency*

As discussed in Section 4.1, BE models must be constructed and solved at each frequency of interest, while the construction of FE models mainly involves computations, which must be performed only once. Table 5 lists the computational loads involved with the three approaches for the *direct IL* and for the *reciprocal IL* calculations. A distinction is made between the variable CPU times, for operations which must be repeated for each frequency, and the fixed CPU times, for operations which must be performed only once. Note that in the first step of the *direct IL* calculations with the semi-coupled and with the uncoupled approach, the postprocessing calculation to determine the blocked pressures from the single and double layer potentials, takes relatively long. Because of this inefficient but unavoidable step, the fully coupled approach turns out to be the most time efficient one. However, when looking at the memory resources required to perform the different analyses (see Table 6), the semi-coupled approach is to be preferred over the

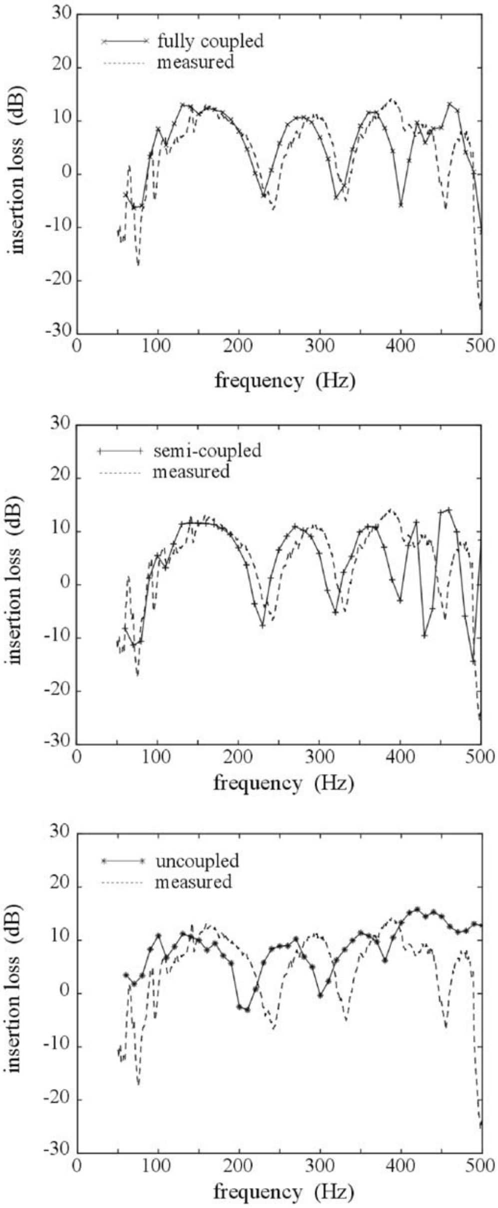

Fig. 26. Cabin scale model reciprocal power insertion loss (dashed line: measured, solid line: predicted (upper: fully coupled, middle: semi-coupled, lower: uncoupled)).

fully coupled approach, since the subsequent calculations in the semi-coupled approach allocate only half of the memory needed for the fully coupled analysis.

In the lower half of Table 5, the CPU times for the *reciprocal IL* calculations are listed. The postprocessing step to calculate the blocked pressure in the semi- and uncoupled approaches is not required, since all necessary information is transferred via normal velocity distributions, which are

Table 5
Computational loads (in seconds CPU time)

	Fully coupled	Semi-coupled	Uncoupled
Direct IL			
Fixed loads			
Acoustic modes		125	125
Structural modes	225	225	225
Coupling matrix $\mathbf{K}_c$ in Eq. (19)		200	
Coupling matrix $\mathbf{L}_c$ in Eq. (16)	5		
Variable loads			
Step 1	300	208	208
Building | solving	160 | 140	131 | 77	131 | 77
Blocked pressure/velocity in BEM		200	200
Step 2		10	0.5
Building | solving		2 | 8	0.1 | 0.4
Step 3			0.6
Building | solving			0.1 | 0.5
Total time for 171 frequencies	51 530	72 028	70 306
Reciprocal IL			
Fixed loads			
Acoustic modes		125	125
Structural modes	225	225	225
Coupling matrix $\mathbf{K}_c$ in Eq. (19)		200	
Coupling matrix $\mathbf{L}_c$ in Eq. (16)	5		
Variable loads			
Step 1	300	10	0.6
Building | solving	160 | 140	2 | 8	0.1 | 0.5
Blocked pressure/velocity in BEM			
Step 2		208	0.5
Building | solving		131 | 77	0.1 | 0.4
Step 3			208
Building | solving			131 | 77
Total time for 171 frequencies	51 530	37 828	36 106

directly available from the structural FE model. This increases the efficiency of the semi- and uncoupled approaches and they become more efficient than the coupled approach.

As mentioned in Section 4, the FE system matrices (5) are large, symmetric, sparsely populated, banded matrices with real coefficients, while the BE system matrix (15) is a small but fully populated matrix with complex coefficients, which are obtained from more tedious numerical

Table 6
Memory resources (in Mb)

	Fully coupled	Semi-coupled	Uncoupled
Step 1	224	136	136
Step 2		100	64
Step 3			28

integrations. The CPU times needed in the different analyses to build and solve the models, reflect these system matrix properties. In a FE analysis, the bulk part of the time is spent in solving the large system of equations, while in a BE analysis, the CPU time needed to construct the system of equations takes a significant part of the total CPU time (see Table 5).

Besides the computational efforts, the human efforts, involved with generating the element meshes, should not be disregarded in this framework. The fully coupled approach requires only the generation of a boundary surface mesh, which may serve both as a structural FE and an acoustic BE mesh, while the semi-coupled and uncoupled approaches require also the generation of a cavity volume mesh which is compatible with the structural FE mesh.

It can be concluded from the figures in Section 5.4 and from Tables 5 and 6 that the calculation of the *IL* via the reciprocal procedure using the semi-coupled approach, provides the best balance between prediction accuracy and computational load. This approach is applied to a real harvester driver's cabin in the next section.

6. Cabin validations

6.1. Preliminary considerations

From the scale model calculations, the semi-coupled approach turns out to give accurate results with reasonable computational efforts, especially when the *reciprocal IL* definition is used. Therefore, this modelling approach will be applied for the case of the real harvester driver's cabin. The semi-coupled approach is also preferred to the fully coupled approach because of the geometrical complexity of the cabin. The roof, for instance, is a three-layered structure with a lot of stiffeners and an internal airconditioning system. Fig. 27 shows the structural FE mesh, which can also serve as BE mesh, for the entire cabin, consisting of 14 796 nodes and 30 488 elements. However, since the BE calculations are the most computationally demanding calculations, it is good practice to keep the BE models as small as possible. By applying the semi-coupled approach to determine the *reciprocal IL*, only the outer structure needs to be included in the BE model, since this is the only part which will radiate sound towards the environment. This more simple BE mesh is shown in Fig. 28 and consists of 8529 nodes and 17 070 elements, a size reduction with a factor of two compared with the BE mesh required for a fully coupled analysis.

As determined in the scale model analysis, the accuracy difference between the pulsating panel and the free-field source strength method to characterize the acoustic source is small, even at the acoustic resonance frequencies of the cabin. Because of this small difference and since, from a

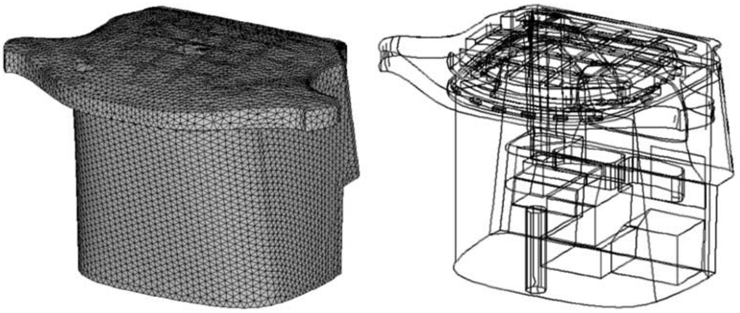

Fig. 27. Cabin structural FE mesh.

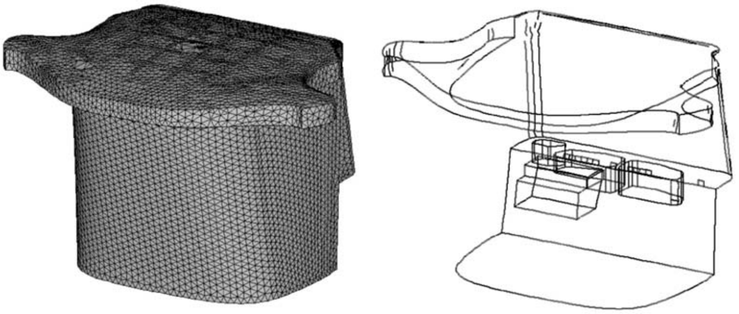

Fig. 28. Cabin acoustic BE mesh.

modelling point of view, the free-field source strength characterization is easier to apply, the latter is used to model the acoustic source inside the cabin in view of determining the *reciprocal IL*.

In the numerical simulations of the cabin, a semi-anechoic nature of the environment is assumed by using the modified Green function G_H (22). In contrast with the cabin scale model, however, the validation measurements on the real harvester cabin have not been performed in a semi-anechoic room.

As mentioned in the previous section, the human efforts involved with generating the element meshes, should not be disregarded. Because of the complex geometry of the real harvester driver's cabin, the creation of the structural FE mesh and especially the creation of the acoustic FE mesh are very labour intensive. The creation of the meshes is further complicated by the fact that, for the considered semi-coupled approach, the acoustic and structural meshes should be compatible at the interface locations in order to allow an accurate modelling of the continuity of the normal fluid and structural displacements along the fluid–structure interface. This compatibility is expressed by the fact that the nodes of the structural FE mesh must coincide with the outer nodes of the acoustic FE mesh.

6.2. Numerical models

The structural FE model of the harvester driver's cabin (see Fig. 27) consists of three-noded plate elements and two-noded beam elements. The trimming and the three-layered roof structure

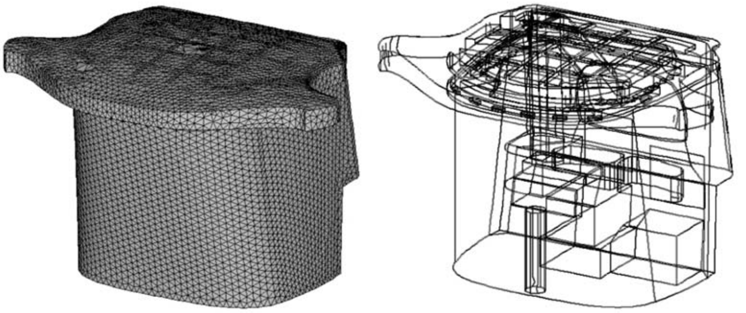

Fig. 29. Cabin acoustic FE mesh.

with integrated airconditioning system, are modelled with as much detail as possible since they may have an influence on the vibro-acoustic behaviour of the cabin. The discretization yields a structural FE model with a total of 89 184 unconstrained degrees of freedom. According to expression (23), this model may provide accurate results up till 200 Hz. In all calculations, a modal projection of type (17) is used for the displacements. The modal base consists of 1500 structural modes with resonance frequencies up till 350 Hz, to which a modal hysteretic damping η_s of 0.03 is assigned.

The acoustic FE model (see Fig. 29) consists of 275 133 four-noded volume elements with 57 379 unconstrained nodal degrees of freedom. The acoustic modal database used for a projection of type (20) consists of 250 uncoupled modes with natural frequencies ω_a below 560 Hz. Note again, as for the scale model, that the acoustic modal base spans a larger frequency range than the structural modal base to accurately represent the normal displacement continuity along the fluid–structure interface.

For the second step in the semi-coupled calculation procedure, an acoustic BE model of the sound radiating surfaces is required (see Fig. 28). As mentioned in Section 6.1, this model consists of 17 070 three-noded linear fluid elements with 8529 acoustic nodes.

6.3. Discussion of results

All uncoupled structural results are obtained with the MSC/NASTRAN v70.7 software, while the acoustic and coupled vibro-acoustic results are obtained with the LMS/SYSNOISE Rev. 5.5 software. All calculations have been performed on an HP-C3000 Unix-workstation (400 MHz single processor, 2.5 Gb RAM, SPECint95 = 31.8, SPECfp95 = 52.4).

Fig. 30 shows the measured and the predicted *IL* in third-octave bands at a point near the driver's left ear for an acoustic source located behind the cabin. Fig. 31 shows the measured and the predicted *IL* in third-octave bands at a point near the driver's left ear for an acoustic source located in front of the cabin. The calculations are based on the reciprocal definition. The acoustic source is modelled with the free-field source strength method. These figures illustrate that the *IL* can be predicted reasonably well.

It may be concluded from the previous figures that the semi-coupled approach is a useful tool to investigate global tendencies in the low-frequency pressure insertion loss.

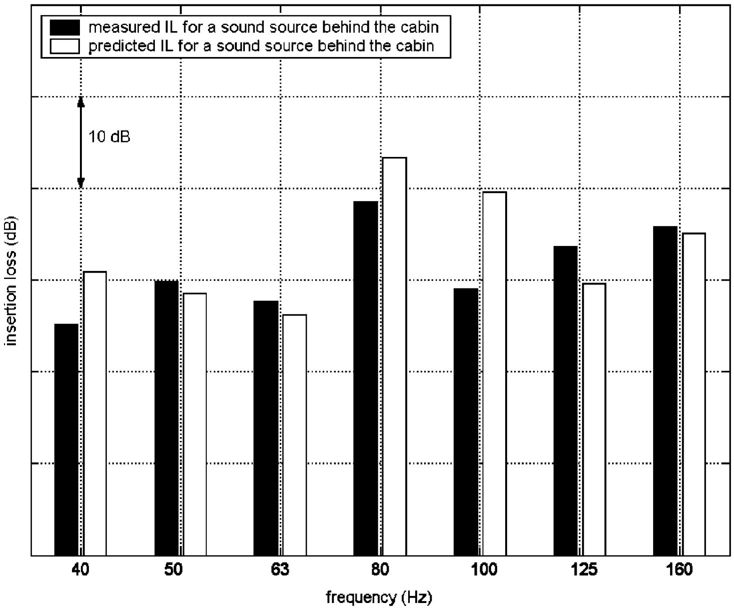

Fig. 30. Reciprocal *IL* in third-octave bands at a point near the driver's left ear for a source located behind the cabin.

Note that, in contrast to the scale model simulations, no model updating has been performed on the uncoupled structural and uncoupled acoustic models of the driver's cabin, so that the obtained insertion loss results can be further improved through dedicated updating procedures.

6.4. Computational efficiency

For the scale model simulations, the semi-coupled modelling approach gave accurate results within a reasonable calculation time. For real-life engineering problems, like the driver's cabin of a harvester, this approach also leads to reasonable results. However, the computational load and the related simulation time increase due to the larger numerical models (see Table 7). Calculating the uncoupled structural and acoustic modal databases takes, respectively, 4412 and 4097 CPU seconds. In the coupled vibro-acoustic FE/FE calculation (step 1 in the semi-coupled approach for the *reciprocal IL* calculation), it takes 26 280 CPU seconds to calculate the coupling matrix $\mathbf{K}_c$ in Eq. (19) and 1143 CPU seconds per frequency in the subsequent frequency response calculation. Step 2 in the semi-coupled approach, which is the uncoupled radiation calculation, based on a BE model, takes 1768 CPU seconds per frequency. Like for the scale model calculations, solving the system of equations takes the larger part in the FE simulation, while in the BE analysis, the larger part of the time is spent on building the system of equations.

In the first step, 1.4 Gb of memory was allocated, while the uncoupled radiation calculation in step 2 required 700 Mb of allocated RAM memory.

Although the computational limit in terms of allocated memory was not yet reached on the considered workstation, these calculations are at the edge of practical efficiency when looking at the required CPU times. Still, the discussed method for predicting the insertion loss characteristics

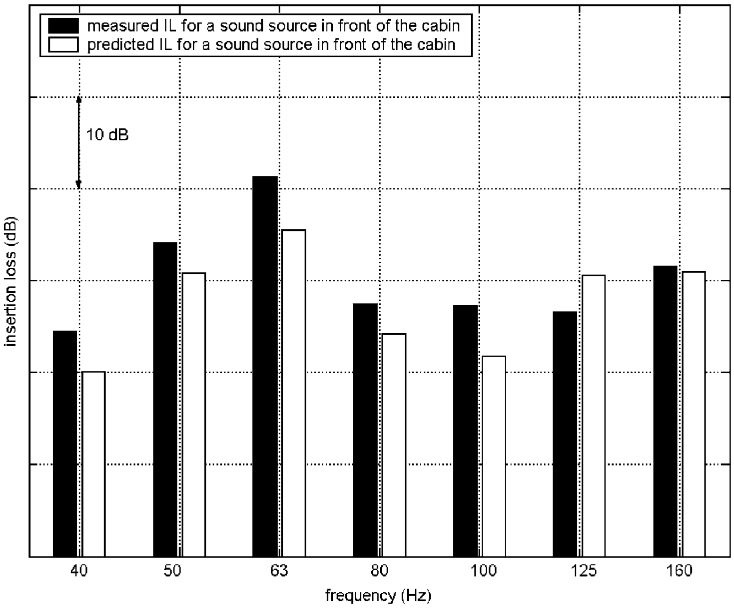

Fig. 31. Reciprocal *IL* in third-octave bands at a point near the driver's left ear for a source located in front of the cabin.

Table 7
Computational loads (in seconds CPU time)

Reciprocal *IL*	Semi-coupled
Fixed loads	
Acoustic modes	4097
Structural modes	4412
Coupling matrix $\mathbf{K}_c$ in Eq. (19)	26 280
Variable loads	
Step 1	1143
Building ∣ solving	298 ∣ 845
Step 2	1768
Building ∣ solving	1070 ∣ 698
Total time for 96 frequencies	314 245 ≈ 87 h

proves to be a useful tool and has a practical applicability in the early design stages of (agricultural) driver's cabins. This may be concluded from the fact that the obtained results have a reasonable accuracy, even when the acoustic and structural numerical models which are used, are just preliminary models which are already available in the early design stages and which have not yet been updated with measurement data. Updated models should be able to predict the *IL* characteristics even more accurately.

7. Conclusions

This paper describes an experimental procedure which can be used for the characterisation of the airborne insertion loss of driver's cabins (of agricultural machinery).

Three numerical modelling approaches, which are based on the finite element and boundary element method, are discussed in terms of their practical use for low-frequency airborne insertion loss predictions. Two source modelling methods are studied and their volume velocity sensitivity to changes in the impedance of the source surroundings is compared.

A reciprocal measurement scheme and calculation procedure for the pressure insertion loss is proposed and validated.

It is concluded from validations on a cabin scale model that the vibro-acoustic coupling with the exterior air may be neglected and that this semi-coupled approach provides a good balance between prediction accuracy and computational load.

The semi-coupled approach has been applied on a real harvester driver's cabin, yielding *IL* predictions with reasonable accuracy. For real-life structures, however, the numerical simulations are still at the edge of practical efficiency when looking at the required CPU times.

Acknowledgements

This research was partly funded by the Belgian Ministry of Small Enterprises, Traders and Agriculture (DG 6). The research work of Bert Pluymers is financed by a scholarship of the Institute for the Promotion of Innovation by Science and Technology in Flanders (IWT).

Appendix. Nomenclature

A	acoustic source strength
c	speed of sound
$\mathbf{C}$	damping matrix
E	Young's modulus
$\mathbf{F}$	force vector
G	Green kernel function
$\mathbf{H}$	model matrix
k	wavenumber
$\mathbf{K}$	stiffness matrix
$\mathbf{M}$	mass matrix
N_a, N_μ	shape function
$\mathbf{\Phi}_a$, $\mathbf{\Phi}_s$	normalized mode
p	acoustic pressure
Q	acoustic volume velocity
q	acoustic volume velocity density
$\mathbf{r}$	position vector
S	surface

t	thickness
v	normal velocity
IL	insertion loss
λ	wavelength
η	hysteretic damping coefficient
ξ	modal viscous damping coefficient
ρ	density
σ, μ	single and double layer potential
ν	Poisson ratio
w	structural displacement
ω	angular frequency

References

[1] ISO 140-3: Acoustics—measurement of sound insulation in buildings and of building elements—part 3: laboratory measurements of airborne sound insulation of building elements, 1995.

[2] F.J. Fahy, The reciprocity principle and application in vibro-acoustics, in: *Proceedings of the Second International Congress on Recent Developments in Air- and Structure-Borne Sound and Vibration*, 1992.

[3] A. Craggs, The use of simple three-dimensional acoustic finite elements for determining the natural modes and frequencies of complex shaped enclosures, *Journal of Sound and Vibration* 23 (1972) 331–339.

[4] A. Craggs, An acoustic finite element approach for studying boundary flexibility and sound transmission between irregular enclosures, *Journal of Sound and Vibration* 30 (1973) 343–357.

[5] M. Petyt, J. Leas, G.H. Koopman, A finite element method for determining the acoustic modes of irregular shaped cavities, *Journal of Sound and Vibration* 45 (1976) 495–502.

[6] P.J.T. Filippi, Layer potentials and acoustic diffraction, *Journal of Sound and Vibration* 54 (1977) 473–500.

[7] A.D. Pierce, X.-F. Wu, Variational method for prediction of acoustic radiation from vibrating bodies, *Journal of the Acoustical Society of America* 74 (Suppl. 1) (1983) S107.

[8] S. Amini, P.J. Harris, A comparison between various boundary integral formulations of the exterior acoustic problem, *Computational Methods in Applied Mechanics and Engineering* 84 (1990) 59–75.

[9] R.A. Jeans, I.C. Mathews, Solution of fluid–structure interaction problems using a coupled finite element and variational boundary element technique, *Journal of the Acoustical Society of America* 88 (1990) 2459–2466.

[10] A.F. Seybert, T.W. Wu, Modified Helmholtz integral equation for bodies sitting on an infinite plane, *Journal of the Acoustical Society of America* 85 (1989) 214–236.

[11] F. Fahy, *Sound Intensity*, Elsevier Applied Science, London, 1989.

[12] F. Jacobsen, Random errors in sound intensity estimation, *Journal of Sound and Vibration* 128 (1989) 247–257.

[13] P. Sas, F. Augusztinovicz, A. Osipov, Pressure gradient acoustic intensity measurements, in: *Proceedings of the* 10*th International Seminar on Applied Acoustics—ISAAC* 10, Leuven, 1999.

[14] ISO 9614-1: Acoustics—determination of sound power levels of noise sources using sound intensity—part 1: measurement at discrete points, 1993.

[15] ISO 9614-2: Acoustics—determination of sound power levels of noise sources using sound intensity—part 2: measurement by scanning, 1996.